Volume 58
Number 73
18 September 2022
Pages 10097–10250

ChemComm

Chemical Communications

rsc.li/chemcomm

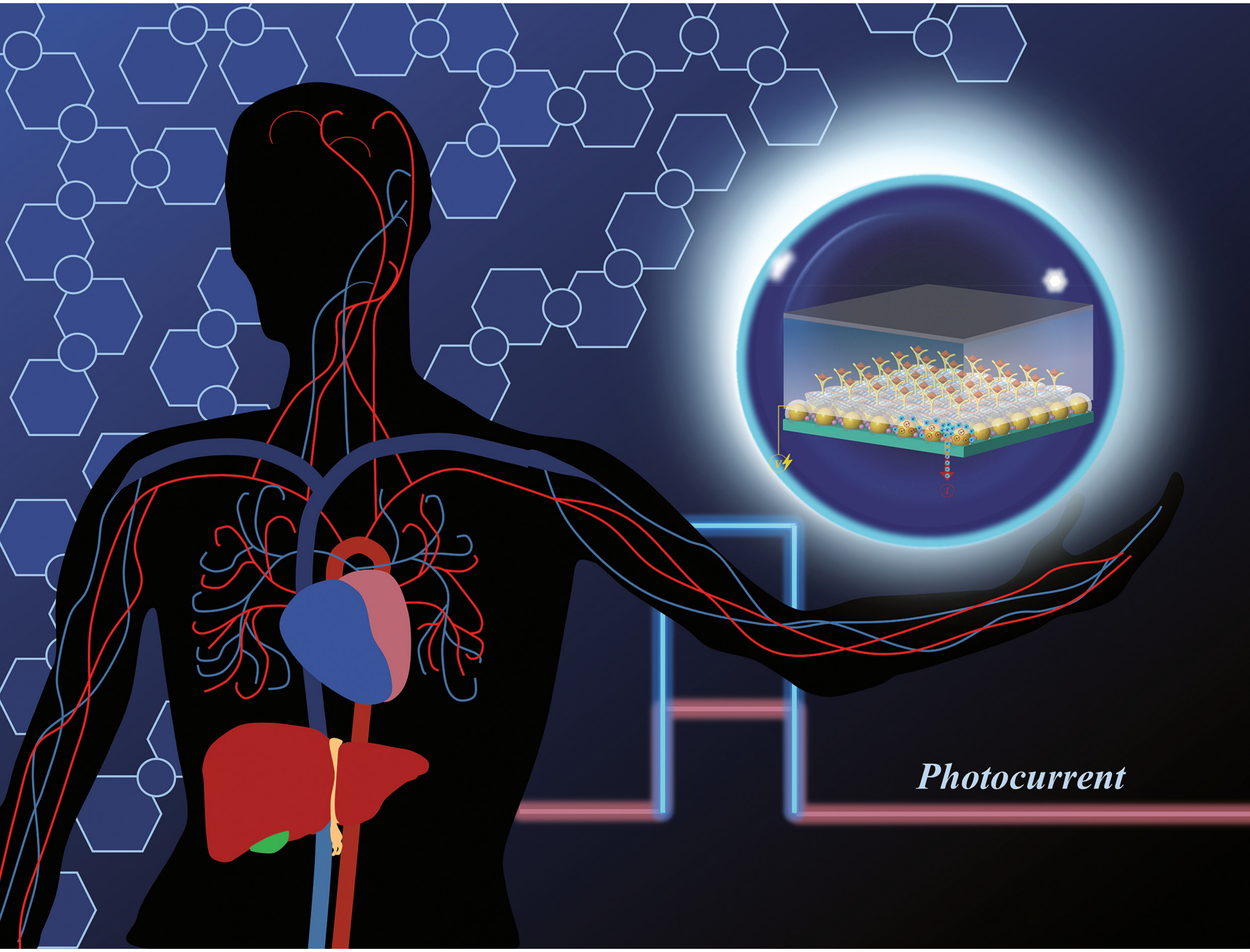

ISSN 1359-7345

ROYAL SOCIETY
OF **CHEMISTRY**

COMMUNICATION
Kuan-Jiuh Lin *et al.*
High-porosity hybrid bilayer-enabled portable LED plasmonic biosensing

ChemComm

ROYAL SOCIETY OF CHEMISTRY

COMMUNICATION

View Article Online
View Journal | View Issue

Cite this: *Chem. Commun.*, 2022, **58**, 10154

Received 6th July 2022,
Accepted 11th August 2022

DOI: 10.1039/d2cc03757b

rsc.li/chemcomm

High-porosity hybrid bilayer-enabled portable LED plasmonic biosensing†

Wen-Yin Ko, ‡ Shin-Chwen Yeh,‡ Hsiao-Wen Chu, Yun-Chen Hsu and Kuan-Jiuh Lin *

A TiO_2-nanowire/Au-nanoparticle hybrid layer, possessing nanocavities and a plasmonic metasurface, can accomplish an entire visible region absorbance, inducing remarkable photocurrent-extraction efficiency. A blood-glucose strip-like testing protocol assembled using this layer allows nondestructive quantitative alpha-fetoprotein detection in human serum under homemade visible LED illumination, indicating its potential in commercial point-of-care testing applications.

Portable light-emitting diode-driven (LED-driven) plasmoelectric biosensors, owing to their inherent plasmonic advantages such as real-time monitoring, label-free detection, high reusability, and short response time,[1–3] have received much attention for healthcare monitoring with the arrival of smart watches and other wearable devices.[4,5] However, it is necessary to develop a stable and efficient plasmonic photoanode that possesses a broadband visible spectrum, large absorption cross sections, superior long-term stability, and facile scale-up fabrication, emerging as strong competition to conventional blood immunosensors.[6–8] One of the issues in these developments is the efficient use of plasmon-derived charge carriers, which will be specific to the plasmonic nano-structural geometry and the nature of metal-interface hybridization. Until now, plasmonic-metal/semiconductor hybrid systems have been considered as the most promising plasmonic materials due to the strong coupling interactions that can drive plasmon-mediated interface-electronic functions for facilitating efficient charge-extraction at visible wavelengths.[9,10] For example, the gap-plasmon nanostructural geometries based on the AuNP/TiO_2/Au-film configuration have been proposed to improve plasmon-derived charge transfer and plasmoelectric conversion.[11,12] These metal–semiconductor–metal architectures provide a first step toward future superior photoelectrodes with the plasmoelectric energy entirely harvested in the visible frequency. However, the usage of this kind of plasmoelectric biosensor in point-of-care testing (POCT) devices for the early detection of viral diseases still remains nascent, owing to the lack of nanopore spatial confinement for the self-assembly of biomolecules.[13–16] For this reason, we propose that semiconductor nanopores combined with light-trigger systems could be extreme auxiliaries for enhancing light-matter interactions in hybrid plasmonic systems.[17,18] To the best of our knowledge, hybrid layers – semiconductor nanopore membranes integrated into surface plasmon-based substrates – are few and far between for plasmonic materials. In this work, we report an ultrasensitive hybrid layer thin film that is made of a TiO_2-nanowire/Au-nanoparticle-plasmonic metasurface with dual functionalities of hybrid broadband absorption property and a nanoporous framework. As a photoanode substrate, we exploit its inherent advantages for boosting efficient charge-extraction behaviors for non-destructive protein detection under homemade visible LED illumination, achieved without the need for a strong laser spot or concentrated solar-light irradiation. It is worth noting that the fabrication involves only simple processes, such as sputtering, alkaline thermal treatment, and annealing, making it easy to fabricate scalable samples at low cost.

Our hybrid photoanode is constructed by a layer-by-layer configuration on glass substrates with a top-layer of highly porous TiO_2 nanowires, a mid-layer of TiO_2-nanowire antennas, and a bottom-layer of densely packed random AuNP-based plasmonic metasurface (HP-TWN/TWA/AuNP-PM), as shown in Fig. 1A. Our previous work has proven that the hot-spot effect of plasmonic substrates is critical and essential to achieve highly efficient plasmon-derived charge-extractions from the arrayed metasurface.[19,20] Therefore, we firstly devoted a lot of efforts to optimizing the synthetic parameters to control the AuNP plasmonic film formation. As shown in the SEM image of Fig. 1B, a large-scale AuNP plasmonic metasurface layer (AuNP-PM), composed by densely randomly packed Au nanoparticles with different Au particle sizes and ultrasmall gap sizes, was formed through the sputtering deposition followed by microwave plasmon heat-treatment (the detailed fabrication process is shown in the ESI†). The corresponding AFM image is shown in Fig. 1C. One can see that the height of the AuNPs ranges from several nanometers to an ∼99 nm final-level with ultrasmall particle

---

Department of Chemistry, National Chung-Hsing University, Taichung 402, Taiwan. E-mail: kjlin@nchu.edu.tw

† Electronic supplementary information (ESI) available. See DOI: **https://doi.org/10.1039/d2cc03757b**

‡ These authors contributed equally to this work.

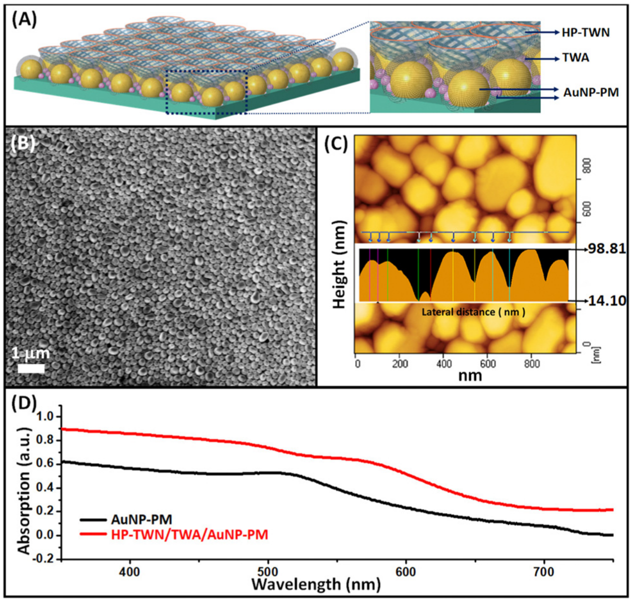

Fig. 1 (A) Schematic configuration of HP-TWN/TWA/AuNP-PM on a glass substrate. (B) SEM image and (C) AFM image of the bottom-layer of the AuNP-PM metasurface film. Inset of (C): the corresponding topographic profile measured along the line in (C). (D) UV-vis spectra of the samples.

gap sizes. During repetition of the deposition/annealing process for Au growth, the Au was deposited several times onto the existing isolated gold nanoparticles produced during the previous thermal annealing treatment. As a result, a unique hierarchical Au multilevel random architecture with different particle thicknesses was fabricated (Fig. 1C). Such an AuNP-multilevel film reveals electro-plasmon characteristics with broad visible wavelength light-harvesting, as illustrated in Fig. 1D. Afterward, an alkaline thermal treatment was applied to fabricate TiO_2 nanowires on the AuNP-PM film. Eventually, after an annealing process, the HP-TWN/TWA/AuNP-PM configuration is accomplished on the glass surface. Its absorption spectrum shows an enhanced absorbance wavelength range and the absorption increases, which is due to the enhanced electric field at the Au–TiO_2 interface.

Cross-sectional structure analysis of the photoanodes is illustrated in Fig. 2. The top-layer HP-TWN layer is indicative of a highly porous and free-standing TiO_2 nanowire structure that is crosswise integrated with the TWA layer. The nest-like cavities in the HP-TWN layer with superior hydrophilicity (red circles in Fig. 2A) can provide a useful biomolecule-loading site for use as an immobilization matrix to facilitate nanoscale biomolecular self-assembly, beneficial for enhancing the biosensors' performance. Another intriguing feature of the HP-TWN/TWA/AuNP-PM film is the TWA mid-layer, that is the TiO_2 nanowire antennas which are uniformly covered on the surface of the AuNPs (cyan dot-curve in Fig. 2A) and can offer intrinsic plasmonic nanoantennas. As confirmed by EDS mapping results (Fig. 2B), the TWA mid-layer shows much higher density distributions of titanium and oxygen elements occupied closely around the surface of the AuNPs, which can provide strong hybrid coupling between the plasmonic metal and semiconductor interface, beneficial for improving plasmon-derived charge transfer and plasmoelectric conversion. The bottom-layer is a AuNP-based plasmonic metasurface with two different Au particle sizes of ~93 nm and ~12 nm in height, which provides an effective hot-spot effect with the TWA film and offers strong adhesive binding capability with substrates (Fig. S1, ESI†). Hence, the HP-TWN/TWA/AuNP-PM film exhibits a remarkable broadband absorption in the visible wavelength range with an enhanced absorption coefficient (Fig. 1D), useful for practical applications in photoelectric detection. In addition, a red shift was observed in the Au peak position, which should not only depend on the dielectric effect. A strong electronic hybridization at the TWA interface should be the dominant effect, which enables plasmon decay from a metal array to a strongly coupled acceptor of semiconductors.[21]

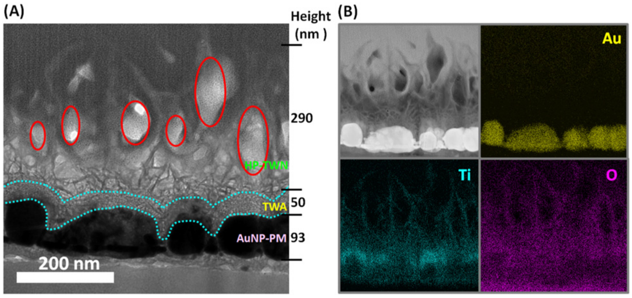

Fig. 2 TEM image (A) and EDS elemental mappings (B) of a cross-section of HP-TWN/TWA/AuNP-HP on a glass substrate.

To verify the photoelectric performance of our plasmoelectric film, a test strip designed with three electrodes, which is the same as a commercial blood glucose strip, is used (Fig. S2, ESI†). For digitalizing portable sensor applications, an accurate and precise measurement of the LED-induced photocurrent based on this plasmoelectric biochip was firstly carried out in 1× phosphate-buffered saline (PBS) solution at an applied potential of 0.0 V (Fig. 3A). Because the energy of the LED light is lower than the bandgap of TiO_2, the photoresponse induced in HP-TWN/TWA/AuNP-PM shown in Fig. 3A is believed to be ascribed to the plasmon-participating photoresponse.[22] The mechanism of photocurrent generation is illustrated in Fig. S3 (ESI†). The present on/off ratio of the HP-TWN/TWA/AuNP-PM electrode is about 35, whereas the AuNP-PM one is relatively low, clearly indicating its high sensitivity for optoelectric detection. Impressively, remarkable 14-fold enhancement in the photocurrent density is observed in the HP-TWN/TWA/AuNP-PM (2.29 $\mu A\ cm^{-2}$), as compared to the one without TiO_2 nanopores (0.16 $\mu A\ cm^{-2}$), due to its better incident-photon-to-current-carrier efficiency resulting from the enhanced separation of plasmonically generated hot electrons at the gold/TiO_2 interface.[23] Such superior photosensitivity illustrates that the use of a LED light source is sufficient to drive the plasmon-electron carriers across a broad range of photo energy, beneficial for portable device usage.

Also, we recorded the dependence of photocurrent generation at different bias voltages, as reported in Fig. 3B. Since plasmon electrons can obtain sufficient energy and momentum to overcome the limitations of the Schottky barrier at the TiO_2/Au interface on increasing the applied voltage, it can enable more efficient photocurrent extraction. It is observed that as the photocurrent generation increases from 0.2 V to 0.6 V, the photocurrent response would

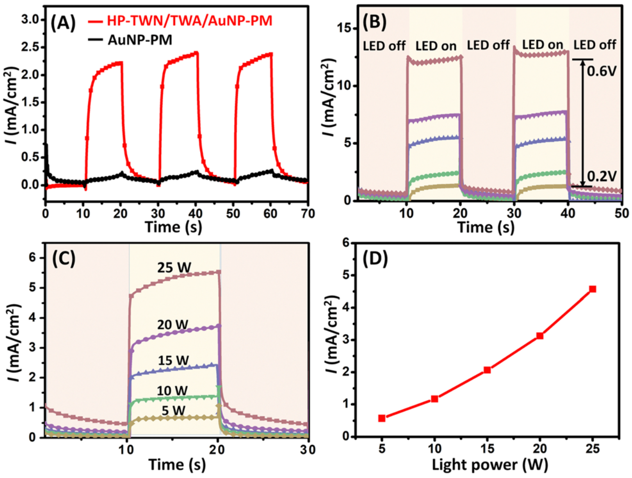

Fig. 3 (A) Photocurrent response collected at 0 V *vs.* Ag/AgCl in PBS solution. (B) Photocurrent response of the device at different bias voltages. (C) Photocurrent response under LED light illumination with different powers at 0.4 V. (D) Relationship between photocurrent and LED light power measured at 0.4 V.

rapidly increase at higher bias voltage; however, it would be limited at bias voltages over 0.5 V due to the surface reaction and oxygen evolution, which may break the film structure and inactivate the biomolecule (Fig. S4, ESI†). Thus, for maintaining the duration of these HP-TWN/TWA/AuNP-PM biochips, an appropriate bias voltage of 0.4 V was chosen. Fig. 3C shows the photo-response of the plasmoelectric detector to light with a LED-power of 0.4 V, where the on–off interval of the light is 5 s. Our device clearly displays a rapid response to the pulsed light. Furthermore, the photocurrent of the device demonstrates a linear-like relationship with the incident LED-light power. The positive slope of the photo-responsivity can be explained in terms of strong symmetry-adapted electronic interactions at the interface, enabling surface trap state passivation during plasmon decay. Besides, all the measurements are reproducible and repeatable, presenting potential in practical applications.

To get an insight into the self-improving performance of protein bilayer formation on the designed HP-TWN/TWA/AuNP-PM biochip, non-destructive infrared (IR) plasmonic resonance studies were performed.[17,24–26] The corresponding schematic model of the as-fabricated hybrid layer photoanode to monitor the proteins adsorbing under IR-driven surface plasmon resonance is presented in Fig. 4A, which describes the following key factors for efficient use in protein characterizations. First, the intrinsic TiO_2/Au dipole-antennal array with hot-spot benefits will enhance the light interaction with protein molecules, and subsequently yield very strong electromagnetic fields that can be capable of absorbing all-incident photons across the IR-spectrum. Second, the hydrophilic TiO_2 nest-like nanocavities (blue bowl) could act as spatial confinement to increase the strength of the plasmonic light concentration and an extremely powerful auxiliary to facilitate the nanoscale biomolecular self-assembly due to the radical-induced dipole interaction upon protein immobilization. Accordingly, plasmoelectric immunosensors are facilely constructed by a one-step process involving the incubation of AFP-antibody protein (1 ppm) on the surface of the biochips for 10 min at ambient temperature without the need for integrating bio-linkers in advance for protein engineering. The corresponding mid-IR spectrum is shown in Fig. 4B. The detection of the protein bilayer is monitored by detecting the plasmon resonance change of the two main vibrational fingerprints of protein molecules, the vibrational fingerprints of amide I and II, in which the absorption peak at 1689 cm^{-1} is attributed to the C=O stretching vibration mode of amide I bonds, and the peak located at 1508 cm^{-1} corresponds to the N–H bending modes of amide II bonds, respectively. It is evident from the data that a red shift of the plasmon resonance is observed in both amide vibrations after antigen-antibody recognition. There is a 68 cm^{-1} redshift for amide I bonds and a 64 cm^{-1} redshift for amide II bonds when the antigen is complexed with the antibody, which is ascribed to a consequence of the change in the refractive index at the sensor surface. The results unambiguously show that mid-IR plasmonic spectra provide an alternative to monitor the presence of a protein bilayer in a non-destructive, label-free, and chemically specific manner by exploiting dipole-induced plasmonic antennas. Further sophisticated IR-mapping measurements for exploring the quantitative detection of protein molecules at low concentration ($<$1 ppm) are undertaken.

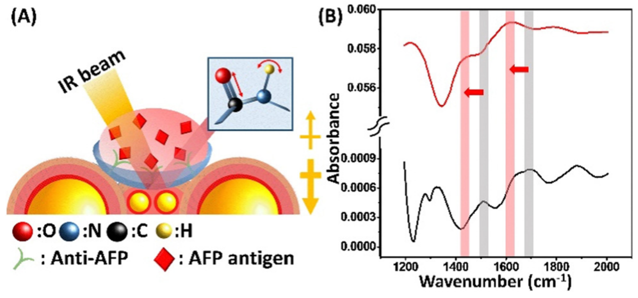

Fig. 4 (A) A conceptual view of the mid-infrared (IR) plasmonic spectrum for protein layer formation. (B) Mid-IR spectra of the plasmonic biochips before (black) and after (red) antigen-antibody recognition.

We believe that this HP-TWN/TWA/AuNP-PM biochip with unique intrinsic plasmonic characteristics and hydrophilic nanopore functionalities can open the way for exploiting a LED-driven immunosensor towards portable detection of proteins for POCT applications; hence the chemically specific label-free quantitative detection of alpha-fetoprotein (AFP) in human serum is executed. Detection for the quantitative analysis of AFP protein was directly examined by monitoring the photocurrent change at an applied potential of 0.4 V under visible LED-light illumination (Fig. S5, ESI†) after the incubation of the biochip in 1000 ppb anti-AFP for 10 min and then in AFP antigen for 30 min (Fig. S6, ESI†). The developed immunosensor was applied to detect different concentrations of AFP in human serum with the photocurrent change under the optimized conditions. The photocurrent intensity change was proportional to the logarithm of the AFP concentration in the wide range from 0.01 ppb to 400 ppb with the regression equation ΔID ($\mu A\ cm^{-2}$) = 0.422 $\log C$ (ppb) + 1.601 and correlation coefficient of 0.995 (Fig. 5A). A short analysis time $<$35 min and a low detection limit of 0.01 ppb were achieved.

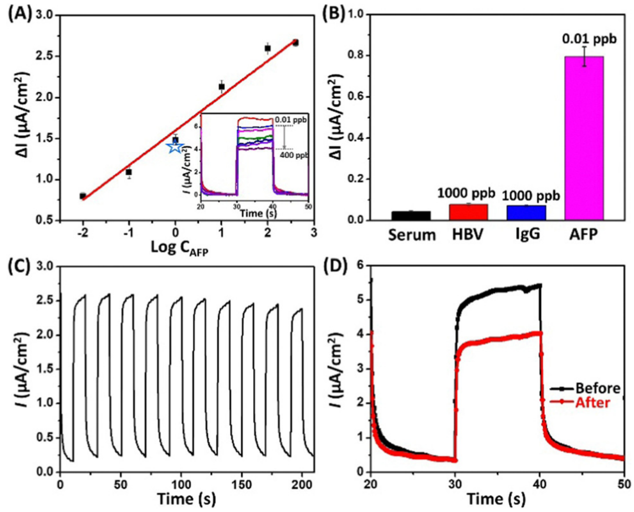

Fig. 5 (A) Photocurrent responses of the immunosensor treated with various AFP concentrations. (B) Selectivity test. Error bars indicate the standard deviation from three samples. (C) Stability evaluation of the immunosensor, C_{AFP} = 400 ppb. (D) Photocurrent change for the immunosensors before and after hybridization with unknown concentrations of AFP in human serum without a wash step. The unknown sample contains about 1.0 ppb AFP antigen in human serum.

To evaluate the specificity of the proposed immunosensor, the response of 1000 ppb IgG and 1000 ppb HBV protein on this sensor was compared to that of the AFP antigen at 0.01 ppb, as illustrated in Fig. 5B. No distinct change in photocurrent was obtained for HBV and IgG in comparison with the result observed in the presence of AFP, which illustrated good selectivity and specificity of the immunosensor for AFP. The stability of the photocurrent response of the fabricated immunosensor is shown in Fig. 5C. After 10 on/off irradiation cycles, the photocurrent response still maintained ~94% of its initial value, indicative of its acceptable stability. Direct detection of the photocurrent change for the immunosensors before and after hybridization with an unknown concentration of AFP antigen in human serum with 30 min incubation time accompanied by no washing step was also performed. The unknown sample data point given by the intercept divided by the slope in (A), which was indicated with a star, demonstrated the good fit for the standard curve. Thus, this hybrid bilayer-based immunosensor represents a straightforward sensing platform for the sensitive and selective detection of target molecules, providing practical applications for AFP detection in clinical diagnosis.

In summary, our work illustrates a hybrid layer photoanode composed of TiO_2-nanowires integrated into an Au-nanoparticle plasmonic metasurface possessing nanopore-functionalities and hybrid-plasmonics characteristics, which has the capability of reaching the goal of direct label-free detection of protein molecules in real time under visible LED illumination. It opens a straightforward sensing route to sensitively and selectively detect target molecules and paves a new avenue for biochip design with minimal integration, beneficial for building a simple POCT module for healthcare monitoring.

This work was supported by the National Science and Technology Council (NSTC), Taiwan (111-2113-M-005-023-, 110-2113-M-005-008-).

Conflicts of interest

There are no conflicts to declare.

Notes and references

1 A. M. Shrivastav, U. Cvelbar and I. Abdulhalim, *Commun. Biol.*, 2021, **4**, 70.
2 C. Lee, B. Lawrie, R. Pooser, K.-G. Lee, C. Rockstuhl and M. Tame, *Chem. Rev.*, 2021, **121**, 4743–4804.
3 J. R. Mejia-Salazar and O. N. Oliveira, *Chem. Rev.*, 2018, **118**, 10617–10625.
4 J. Kim, A. S. Campbell, B. E.-F. de Ávila and J. Wang, *Nat. Biotechnol.*, 2019, **37**, 389–406.
5 Y. Wang, C. Zhao, J. Wang, X. Luo, L. Xie, S. Zhan, J. Kim, X. Wang, X. Liu and Y. Ying, *Sci. Adv.*, 2021, **7**, eabe4553.
6 C. Ng, J. J. Cadusch, S. Dligatch, A. Roberts, T. J. Davis, P. Mulvaney and D. E. Gómez, *ACS Nano*, 2016, **10**, 4704–4711.
7 F. Qin, L. Ding, L. Zhang, F. Monticone, C. C. Chum, J. Deng, S. Mei, Y. Li, J. Teng, M. Hong, S. Zhang, A. Alù and C.-W. Qiu, *Sci. Adv.*, 2016, **2**, e1501168.
8 Z. Yue, B. Cai, L. Wang, X. Wang and M. Gu, *Sci. Adv.*, 2016, **2**, e1501536.
9 S. Linic, S. Chavez and R. Elias, *Nat. Mater.*, 2021, **20**, 916–924.
10 K. Wu, J. Chen, J. R. McBride and T. Lian, *Science*, 2015, **349**, 632–635.
11 X. Shi, K. Ueno, T. Oshikiri, Q. Sun, K. Sasaki and H. Misawa, *Nat. Nanotechnol.*, 2018, **13**, 953–958.
12 Y. Lu, W. Dong, Z. Chen, A. Pors, Z. Wang and S. I. Bozhevolnyi, *Sci. Rep.*, 2016, **6**, 30650.
13 W.-Y. Ko, T.-J. Tien, C.-Y. Hsu and K.-J. Lin, *Biosens. Bioelectron.*, 2019, **126**, 455–462.
14 S. Mariani, V. Robbiano, L. M. Strambini, A. Debrassi, G. Egri, L. Dähne and G. Barillaro, *Nat. Commun.*, 2018, **9**, 5256.
15 J. P. Fried, J. L. Swett, B. P. Nadappuram, A. Fedosyuk, P. M. Sousa, D. P. Briggs, A. P. Ivanov, J. B. Edel, J. A. Mol and J. R. Yates, *Small*, 2021, **17**, 2102543.
16 B. M. Venkatesan and R. Bashir, *Nat. Nanotechnol.*, 2011, **6**, 615–624.
17 X. Yang, Z. Sun, T. Low, H. Hu, X. Guo, F. J. García de Abajo, P. Avouris and Q. Dai, *Adv. Mater.*, 2018, **30**, 1704896.
18 J.-Z. Chen, W.-Y. Ko, Y.-C. Yen, P.-H. Chen and K.-J. Lin, *ACS Nano*, 2012, **6**, 6633–6639.
19 Y.-C. Yen, P.-H. Chen, J.-Z. Chen, J.-A. Chen and K.-J. Lin, *ACS Appl. Mater. Interfaces*, 2015, **7**, 1892–1898.
20 Y.-C. Yen, J.-A. Chen, S. Ou, Y.-S. Chen and K.-J. Lin, *Sci. Rep.*, 2017, **7**, 42524.
21 N. Wu, *Nanoscale*, 2018, **10**, 2679–2696.
22 F. Tan, N. Wang, D. Y. Lei, W. Yu and X. Zhang, *Adv. Opt. Mater.*, 2017, **5**, 1600399.
23 L. J. Brennan, F. Purcell-Milton, A. S. Salmeron, H. Zhang, A. O. Govorov, A. V. Fedorov and Y. K. Gun'ko, *Nanoscale Res. Lett.*, 2015, **10**, 38.
24 I. Amenabar, S. Poly, W. Nuansing, E. H. Hubrich, A. A. Govyadinov, F. Huth, R. Krutokhvostov, L. Zhang, M. Knez, J. Heberle, A. M. Bittner and R. Hillenbrand, *Nat. Commun.*, 2013, **4**, 2890.
25 O. Limaj, D. Etezadi, N. J. Wittenberg, D. Rodrigo, D. Yoo, S.-H. Oh and H. Altug, *Nano Lett.*, 2016, **16**, 1502–1508.
26 D. Rodrigo, O. Limaj, D. Janner, D. Etezadi, F. J. G. D. Abajo, V. Pruneri and H. Altug, *Science*, 2015, **349**, 165–168.